International Journal of Nanomedicine

Dovepress
open access to scientific and medical research

Open Access Full Text Article

ORIGINAL RESEARCH

Gold Nanorod-Loaded Nano-Contrast Agent with Composite Shell-Core Structure for Ultrasonic/Photothermal Imaging-Guided Therapy in Ischemic Muscle Disorders

Xiaoyi Tang[1,2,*], Yijia Liu[1,2,*], Mengxin Zhao[3,*], Lei He[3], Jiahao Guo[3], Tian Wang[3], Wei Li[3], Jiaqi Zhao[1]

[1]Department of Ultrasound, Shanghai Fourth People's Hospital, School of Medicine, Tongji University, Shanghai, 200434, People's Republic of China; [2]Department of Ultrasound, the Second Affiliated Hospital of Naval Medical University (Shanghai Changzheng Hospital), Shanghai, 200003, People's Republic of China; [3]Department of Nanomedicine, Naval Medical University, Shanghai & School of Health Science and Engineering, University of Shanghai for Science and Technology, Shanghai, 200433, People's Republic of China

*These authors contributed equally to this work

Correspondence: Wei Li; Jiaqi Zhao, Email liwei@smmu.edu.cn; ultrasoundczzjq@163.com

Purpose: This study aims to broaden the application of nano-contrast agents (NCAs) within the realm of the musculoskeletal system. It aims to introduce novel methods, strategies, and insights for the clinical management of ischemic muscle disorders, encompassing diagnosis, monitoring, evaluation, and therapeutic intervention.

Methods: We developed a composite encapsulation technique employing O-carboxymethyl chitosan (OCMC) and liposome to encapsulate NCA-containing gold nanorods (GNRs) and perfluoropentane (PFP). This nanoscale contrast agent was thoroughly characterized for its basic physicochemical properties and performance. Its capabilities for in vivo and in vitro ultrasound imaging and photothermal imaging were authenticated, alongside a comprehensive biocompatibility assessment to ascertain its effects on microcirculatory perfusion in skeletal muscle using a murine model of hindlimb ischemia, and its potential to augment blood flow and facilitate recovery.

Results: The engineered GNR@OCMC-liposome/PFP nanostructure exhibited an average size of 203.18±1.49 nm, characterized by size uniformity, regular morphology, and a good biocompatibility profile. In vitro assessments revealed NCA's potent photothermal response and its transformation into microbubbles (MBs) under near-infrared (NIR) irradiation, thereby enhancing ultrasonographic visibility. Animal studies demonstrated the nanostructure's efficacy in photothermal imaging at ischemic loci in mouse hindlimbs, where NIR irradiation induced rapid temperature increases and significantly increased blood circulation.

Conclusion: The dual-modal ultrasound/photothermal NCA, encapsulating GNR and PFP within a composite shell-core architecture, was synthesized successfully. It demonstrated exceptional stability, biocompatibility, and phase transition efficiency. Importantly, it facilitates the encapsulation of PFP, enabling both enhanced ultrasound imaging and photothermal imaging following NIR light exposure. This advancement provides a critical step towards the integrated diagnosis and treatment of ischemic muscle diseases, signifying a pivotal development in nanomedicine for musculoskeletal therapeutics.

Keywords: ultrasonography, nanoscale contrast agent, nanotechnology, musculoskeletal ultrasound, photothermal imaging, microcirculatory perfusion

Introduction

Skeletal muscle is the most susceptible tissue to ischemia, with microcirculatory dysfunction recognized as a crucial early event in ischemic muscle injury.[1] Microcirculation injury, particularly in skeletal muscle of the lower limbs, is closely associated with the progression of peripheral vascular disease and diabetic lower limb lesions.[2] When ischemic injury occurs in skeletal muscle, early clinical manifestations may not be obvious, there is a notable absence of validated methods for

Received: 8 November 2023
Accepted: 12 April 2024
Published: 8 May 2024

effective evaluation of microcirculation at the muscle extremities. Traditional macrovascular perfusion assessments, such as color Doppler flow imaging (CDFI), do not adequately capture microvascular perfusion in skeletal muscle. Consequently, non-invasive and real-time imaging techniques that can accurately evaluate skeletal muscle microcirculatory perfusion are essential for the early detection, diagnosis, and treatment efficacy assessment of limb and muscle ischemic injuries.

Studies have demonstrated the potential of ultrasonography as an effective tool for monitoring muscle involvement, regenerative processes, and the efficacy of anti-inflammatory treatments.[3,4] Conventional microbubble (MB) ultrasound contrast agents (UCAs), with their micron-scale size, predominantly facilitate blood pool imaging, given their average diameter spanning approximately 2–4 μm. However, recent advancements in nanotechnology have led to the emergence of various nano-contrast agents (NCAs). These NCAs, through their ability to dynamically quantify microcirculatory perfusion in muscle tissues, offer a lens into the flow field characteristics within both deep and superficial tissues, including articular vessels.[5,6] Exploring and applying NCAs promises to revolutionize the diagnosis and treatment of musculoskeletal disorders.

Additionally, nano-photothermal therapy has emerged as a significant advancement in biological therapy, notable for its wide applicability, selectivity, and operational ease.[7] As a traditional treatment, thermal therapy inflicts minimal damage to normal tissues and is a mainstay in managing various chronic diseases, earning its place as a primary therapy in rehabilitation sports medicine. However, the efficacy of traditional thermal therapy is hampered by low heat transfer efficiency and limited therapeutic outcomes. The introduction of nano-photothermal therapy offers a solution to these limitations,[8] demonstrating encouraging results in musculoskeletal tissue rehabilitation.[9,10] Nano-photothermal agents, particularly gold nanostructures, are favored for their unique optical properties, which enable strong absorption of near-infrared (NIR) light, allowing for effective tissue penetration and adjustment of structure size.[11,12] Different forms exhibit varying photothermal conversion efficiencies;[13] Gold nanorods (GNRs), with their distinctive surface plasmon resonance (SPR) properties, have attracted attention for tumor photothermal therapies due to their efficient light absorption and conversion into localized heat.[14] While various nanoparticles (NPs) have been explored for musculoskeletal treatments, GNRs stand out for their broad potential in tissue engineering and regenerative medicine, attributed to their low toxicity, straightforward synthesis, and excellent biocompatibility.[15]

This study aims to develop a bimodal NCA that integrates ultrasonic and photothermal modalities. The strategy involves synthesizing o-carboxymethyl chitosan (OCMC) NPs through the copolymerization of OCMC with methyl methacrylate (MMA), followed by crafting GNR@OCMC-liposome/PFP composites via pulsed ultrasound, incorporating liposomes, GNRs, and perfluoropentane (PFP). By performing NIR light irradiation during ultrasonography of ischemic skeletal muscles, it is anticipated that SPR-induced heat generation by GNRs and enhanced blood circulation at the irradiated site will promote tissue recovery (Figure 1). These efforts are expected to establish a foundation for the integrated diagnosis and treatment of ischemic muscle diseases.

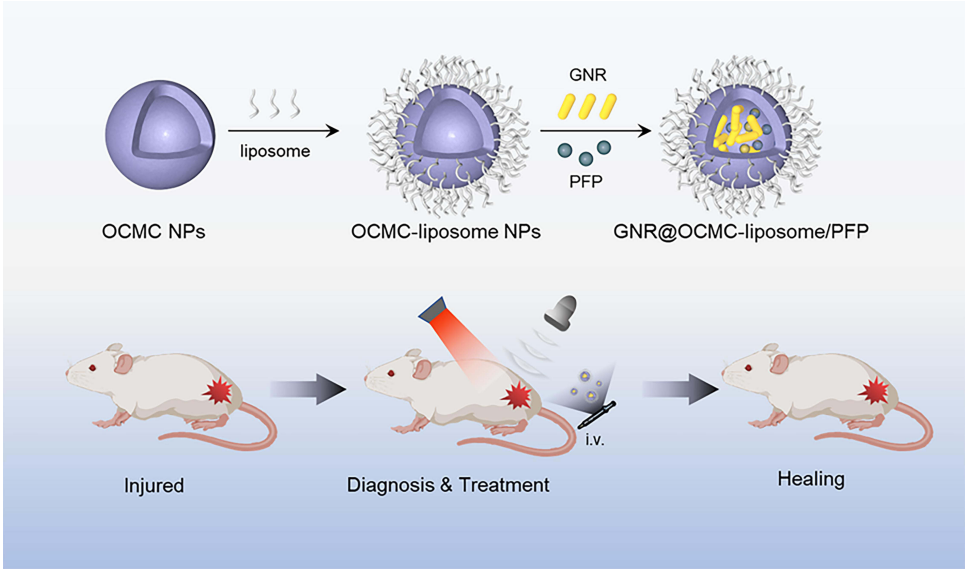

Figure 1 Schematic of the preparation and the image-guided treatment.

Materials and Methods

Materials

The following chemicals were procured from Sigma Aldrich (MO, USA): silver nitrate ($AgNO_3$), sodium borohydride ($NaBH_4$), hydrogen tetrachloroaurat(III) ($HAuCl_4$), L-ascorbic acid, and cetyltrimethylammonium bromide (CTAB). Additionally, the following chemicals were obtained from Sinopharm Chemical Reagent Co., Ltd. (Shanghai, China): Methyl methacrylate (MMA), Ammonium persulfate (APS), Palmitoyl oleyl Phosphatidylcholine (POPC), and Agarose. Phosphate Buffered Saline (PBS) and Fetal Bovine Serum (FBS) were procured from GIBCO Co., Ltd. (California, USA). Trypsin and high glycemic medium (Dulbecco's modified Eagle's medium, DMEM) were also acquired from GIBCO Co., Ltd. The CCK-8 kit was purchased from MCE (MedChemExpress); Perfluoropentane (PFP) and O-Carboxymethylchitosan (OCMC) were provided by Shanghai Aladdin Biochemical Technology Co., Ltd.

Preparation of GNR@OCMC-Liposome/PFP

A total of 5 g of OCMC was weighed and dissolved in 250 mL of double-distilled water, followed by filtration and transfer into a round-bottom flask. The flask was then heated to 50°C. Subsequently, 1.5 mL of MMA was added to the solution and stirred for 20 minutes, after which 1.5 mL of a 5% APS solution was introduced. The temperature was gradually increased to 70°C whereupon continuous stirring was maintained for an additional 24 hours. The resultant mixture underwent dialysis and lyophilization to yield freeze-dried OCMC NPs. The resultant mixture underwent dialysis and lyophilization to yield freeze-dried OCMC NPs.

For liposome preparation, 1-palmitoyl-2-oleoyl-sn-glycero-3-phosphocholine (POPC) was dissolved in anhydrous ethanol. Subsequently, the solution was transferred into a round bottom flask and subjected to centrifugation at 100 rpm for 10–15 minutes at 37°C to form a thin film. The film was rinsed with PBS and dispersed using ultrasonic treatment, followed by filtration through a 0.45 μm filter membrane and freeze-drying to produce lyophilized liposome powder.

GNRs were synthesized by mixing 5 mL of a $HAuCl_4$ solution to 5 mL of a 200 mM CTAB solution and stirred for 5 minutes. This was followed by the dropwise addition of 0.6 mL of $NaBH_4$ solution (10 mM prepared with ice water) with stirring. The solution underwent a color change from orange-yellow transparent to colorless and finally to tea-brown. After uniform stirring of the precursor mixture for an additional 20 minutes, it was left undisturbed at room temperature for 2–5 hours to serve as the seed solution for subsequent experiments. A new mixture was prepared by combining 5 mL of a 1 mM $HAuCl_4$ solution with 5 mL of a 200 mM CTAB solution, stirred thoroughly for precisely 5 minutes. To this, 750 μL of $AgNO_3$ (final concentration: 4 mM) and 350 μL of ascorbic acid (final concentration: 80 mM) were added slowly, altering the mixture's color to colorless during continuous stirring for an additional 2 to 5 minutes, thus creating the growth solution. The seed solution (50 μL) was then introduced dropwise into the growth medium, causing a transition from colorless to a purple-black hue; this mixture was stirred continuously for 12 hours. Following this, the mixture was centrifuged at approximately 8000 rpm for 10 minutes, the supernatant was carefully removed, and the precipitated GNRs were weighed, volume-adjusted with double-distilled water, and stored at room temperature.

For the formation of the bimodal NCA, OCMC NPs and lyophilized liposome powder were combined in a 1:1 volume ratio of 10 mL each. This mixture underwent polymer formation through pulsed sonication (30 W, on for 3 seconds and off for 3 seconds, for a total of 5 minutes). Following this, 200 μL of PFP and 500 μL of the GNR solution were added dropwise under continuous stirring in light-protected conditions. The mixture was then subjected to sonication in a water bath for 10 minutes. The resultant product was dialyzed against pure water for 12 hours to yield GNR@OCMC-liposome/PFP, which was then lyophilized and stored as a powder at −4°C. For comparative analysis, a parallel control group comprising GNR@OCMC-liposome without PFP was prepared, alongside PBS as a negative control and Sonazoid (GE Healthcare, Oslo, Norway) as a positive control group.

Characterization of GNR@OCMC-Liposome/PFP

Morphological Observation

An aliquot of each sample solution was placed onto a carbon film-coated copper mesh. Excess liquid was removed with filter paper, and the samples were air-dried at room temperature for 3–5 minutes. Transmission electron microscopy (TEM) was employed to examine the samples, with images captured to document the morphology.

Particle Size and Potential Measurement

The sample solutions were analyzed using a particle size analyzer (BeNano 90 Zeta, Dandong, China) to determine their particle size distribution, polydispersity index (PDI), and surface zeta (ζ) potential at 25°C.

Stability Evaluation

The stability of GNR@OCMC-liposome/PFP and Sonazoid, both at a concentration of 5 mg/mL, was monitored over a period of 14 days by observing morphological changes and measuring particle size and PDI on days 1, 2, 3, 7, 10, and 14.

In vitro Cytotoxicity

C2C12 myogenic cells (QuiCell, Shanghai, China) were cultured in 96-well plates at a density of 1×10^4 cells/well and incubated at 37°C in a 5% CO_2 cell culture chamber for 24 hours. The culture medium was then replaced with medium containing varying concentrations of GNR@OCMC-liposome/PFP and Sonazoid. After 24 hours and 48 hours, the cells were washed with PBS and treated with 10% CCK-8 solution for one hour. Absorbance at 450 nm was measured using a multifunctional microplate reader, and cell viability (%) was calculated.

$$Cell\ viability(\%) = \frac{OD_{experimental\ wells-blank\ wells}}{OD_{control\ wells-blank\ wells}} \times 100\%$$

Phase Transition Experiment

The GNR@OCMC-liposome/PFP solution was applied to a slide and subjected to NIR light irradiation (760 nm, 1.0 W/cm^2) at the center, while monitoring the generation of bubbles under a microscope to observe bubble generation with increasing irradiation time.

In vitro Ultrasound/Photothermal Dual-Modality Imaging

Ultrasound Imaging

The ultrasound machine (VINNO G86, Suzhou, China) settings were adjusted for optimal imaging, and NIR laser light (760 nm, 1.0 W/cm^2) was applied for 5 minutes. Imaging enhancement signals were quantified using IMAGE J software. Control groups including PBS, Sonazoid, and GNR@OCMC-liposome underwent similar procedures.

Photothermal Imaging

1.5 mL of PBS along with various concentrations of GNR@OCMC-liposome/PFP were introduced into 2 mL Eppendorf tubes. These samples were then subjected to continuous irradiation for 10 minutes using an NIR laser light source at 760 nm and 1.0 W/cm^2. The temperature changes of each sample group were then observed. In a similar experiment, GNR@OCMC-liposome/PFP at a concentration of 5 mg/mL was irradiated at three different power levels using the 760 nm NIR laser, to document the resultant temperature changes. Then, the real-time temperature dynamics of GNR@OCMC-liposome/PFP within the tubes were monitored, following an established protocol for sample concentration and laser power adjustments (5 mg/mL, 760 nm, 1.0 W/cm^2). Upon reaching peak temperature, the laser was deactivated to allow the samples to naturally return to room temperature before the process was repeated for a total of three cycles. The resultant temperature-time profiles were plotted to clearly illustrate the relationships. Under optimal conditions, the photothermal imaging capability of GNR@OCMC-liposome/PFP was assessed using a thermal imager (FOTRIC 246M-L30-M50, Shanghai, China). For comparative analysis, PBS, Sonazoid, and GNR@OCMC-liposome were also tested in separate 2 mL Eppendorf tubes using similar methods.

In vivo Imaging and Therapy

Male ICR mice, aged 8 weeks and weighing approximately 30 g, were procured from Shanghai Legen Biotechnology Co., Ltd. The experimental protocols were approved by the Institutional Animal Care and Use Committee of the Naval Medical University (20ZR1457900), ensuring compliance with the laboratory animal—guideline for ethical review of animal welfare approved by the People's Republic of China.

Construction of a Mouse Hindlimb Ischemia Model

Mice were anesthetized with a 0.5% sodium pentobarbital solution administered intraperitoneally at 50 mg/kg. The animals were then positioned in supine on a thermostatic plate to maintain body temperature, and the hindlimbs sterilized and prepared for surgery. Using an aseptic technique, an oblique incision was made in the left inguinal region to separate the femoral artery, femoral vein, and femoral nerve. The femoral artery and femoral vein were partially ligated using a 4–0 suture, which was placed 0.5 mm distal to the bifurcation originating from the internal iliac artery. This procedure involved placing a 29G insulin syringe needle (0.33 mm in diameter) between the vessels and the suture, creating intentional gaps to avoid complete occlusion. This technique ensured that the vessels were secured alongside the needle, facilitating controlled blood flow while avoiding total vessel closure. After needle removal, the incision was sutured, establishing a unilateral hindlimb ischemia model, designated as the ischemia group. The contralateral limb served as a control for comparison. Additionally, a sham operation group was included, where mice underwent skin incision followed by suturing without ligation. Pathological analysis of bilateral hindlimb muscles was conducted on days 1 and 7 post-operation to validate model induction.

Ultrasound Imaging of Mouse Skeletal Muscle

The mice were randomly allocated into four groups (n=6): PBS, GNR@OCMC-liposome, GNR@OCMC-liposome/PFP, and Sonazoid. Under anesthesia, the mice were positioned prone, with the left hindlimb secured for ultrasound imaging employing a superficial probe (X4-12L). A consistent longitudinal section was selected with the tibia serving as a bony landmark. Following intravenous injection of each solution (0.1 mL) via the tail vein, in each mouse, the left hindlimb was irradiated with NIR light to enable two-dimensional B-mode and contrast-enhanced ultrasound (CEUS) imaging, which was then stored for subsequent analysis while maintaining consistent experimental conditions.

Photothermal Imaging of Mouse Skeletal Muscle

Similar group allocations were used for photothermal studies. Mice, anesthetized in the prone position, received 0.1 mL injections of the respective solutions. A thermal imager was used to dynamically monitor the hindlimbs under NIR laser irradiation. This setup allowed for the continuous observation of local temperature changes and facilitated quantitative image analysis through dedicated software.

Photothermal Treatment of Ischemic Hindlimbs in Mice

The mice were randomly allocated into 3 groups (n=6): PBS, PBS + laser, and GNR@OCMC-liposome/PFP + laser, for a 7-day photothermal therapy regimen. Following intravenous injection of 0.1 mL of the respective solutions, the mice were irradiated with NIR light for approximately 5 minutes every two days. Prior to each treatment, the general condition of the mice was observed. Evaluations of muscle gross morphology in the affected limbs were conducted preoperatively and postoperatively. Muscle tissues were harvested postoperative day 7 for histological examination using H&E staining, Masson's trichrome staining, CD31 immunohistochemistry and fluorescence staining, with the healthy limbs serving as controls.

In vivo Toxicity

Following the administration of GNR@OCMC-liposome/PFP and PBS, mice were euthanized via cervical dislocation under anesthesia. Heart, liver, spleen, lung, and kidney tissues were promptly collected for histological examination. Additionally, after tail vein injection of solutions from groups GNR@OCMC-liposome/PFP and PBS into normal mice, blood samples were collected after 48 hours for complete blood analysis, assessing GNR@OCMC-liposome/PFP accumulation in parenchymal organs, and evaluating potential in vivo toxicity.

Statistical Analysis

Data were analyzed using GraphPad Prism 9.0.0 software, with measures conforming to a normal distribution were presented as mean ± standard deviation (mean ± SD). Comparisons between the two groups were made using the Student's *t*-tests. One-way ANOVA was used to compare multiple groups. A significance level of $P < 0.05$ was considered indicative of statistical significance.

Results

Preparation and Characterization of GNR@OCMC-Liposome/PFP

Utilizing a Malvern particle size/potential analyzer, precise measurements were obtained for the particle size distribution, PDI, and ζ potential of the GNR@OCMC-liposome/PFP. Table 1 exhibits the comprehensive particle size and potential data across various solution groups, with a focus on comparing GNR@OCMC-liposome/PFP to Sonazoid. The GNR@OCMC-liposome /PFP presented an average particle size of 203.18 ± 1.49 nm, substantially smaller than the Sonazoid average of 2317.80 ± 111.94 nm, highlighting the size advantage of GNR@OCMC-liposome/PFP particles. The PDI, indicative of sample uniformity, revealed that the GNR@OCMC-liposome/PFP had a PDI of 0.32 ± 0.04, suggesting a relatively stable dispersion. The ζ-potential for GNR@OCMC-liposome/PFP was measured at −26.44 ± 1.15 mV, indicating a negatively charged surface conducive to extended circulation times in blood.

The microscopic and macroscopic morphology of the GNR@OCMC-liposome/PFP, as well as GNR, OCMC-liposome/PFP, OCMC/PFP, and Sonazoid are shown in Figure 2A. The synthesized bimodal NCA GNR@OCMC-liposome/PFP appears as a pale pink suspension to the naked eye. Figure 2A depicted regular-shaped and centrally clustered GNRs, and homogeneous OCMC-liposome/PFP, and OCMC/PFP samples. In contrast, Sonazoid displayed a patchwork appearance with disrupted structure under TEM analysis (Figure 2A and Supplementary Figure 1).

Evaluating the stability of GNR@OCMC-liposome/PFP over a 14-day period at 4°C indicated an initial size and PDI reduction, followed by stabilization, highlighting the relative stability of the formulation (Figure 2B). This contrasts with Sonazoid, which although stable for up to 2 days, showed structural degradation beyond day 3, transitioning from milky white to a clear solution. (Supplementary Figure 2A and 2B). The GNR@OCMC-liposome/PFP, however, maintained excellent structural stability (Supplementary Figure 2A). The CCK8 assay revealed cell viability above 80% following incubation of mouse C2C12 cells with various concentrations of GNR@OCMC-liposome/PFP suspensions over 24 hours and 48 hours (Figure 2C and Supplementary Figure 3A). Notably, no significant cytotoxicity was observed even at a high concentration, thus confirming the excellent biocompatibility profile of the GNR@OCMC-liposome/PFP. Similarly, commercially produced Sonazoid also demonstrated a favorable biocompatibility profile (Supplementary Figure 2C and Supplementary Figure 3B).

In vitro Photothermal Properties and Phase Transition Capability

The photothermal efficacy of GNR@OCMC-liposome/PFP was investigated by monitoring temperature elevations using a 760 nm laser at various power densities (0.8 W/cm^2, 1.0 W/cm^2, and 1.2 W/cm^2) and solution concentrations of the GNR@OCMC-liposome/PFP under a power density of 1.0 W/cm^2, using PBS serving as a blank control. Real-time temperature-time curves (Figures 3A and B) illustrated that both laser power and solution concentration influenced the temperature increase in GNR@OCMC-liposome/PFP. Following 5 minutes of irradiation, the solution reached approximately 30°C under a power density of 0.8 W/cm², around 40°C under a power density of 1.0 W/cm², and over 50°C under a power density of 1.2 W/cm². Higher powers resulted in accelerated heating rates. Likewise, increasing solution concentration led to higher heating rates and correspondingly higher maximum temperatures. Cold and thermal cycling experiments further validated high structural and performance stability (Figure 3C). Typically, photothermal treatment for tumors requires maintaining temperatures above 47°C to induce rapid necrosis; however, this approach may damage normal tissues.[16] To achieve both photothermal treatment effectiveness and optical droplet vaporization (ODV), an

Table 1 Particle Size and ζ-Potential Distribution of Each Group of Solutions

Groups	Size ± SD (nm)	PDI ± SD	ζ ± SD (mV)
GNR@OCMC-liposome/PFP	203.18 ± 1.49	0.32 ± 0.04	−26.44 ± 1.15
Sonazoid	2317.80 ± 111.94	0.03 ± 0.01	−65.87 ± 0.86
GNR	50.32 ± 1.80	0.36 ± 0.03	26.08 ± 1.64
OCMC/PFP	153.33 ± 1.11	0.12 ± 0.02	−20.86 ± 0.95
OCMC-liposome/PFP	306.97 ± 8.27	0.25 ± 0.02	−29.74 ± 0.54

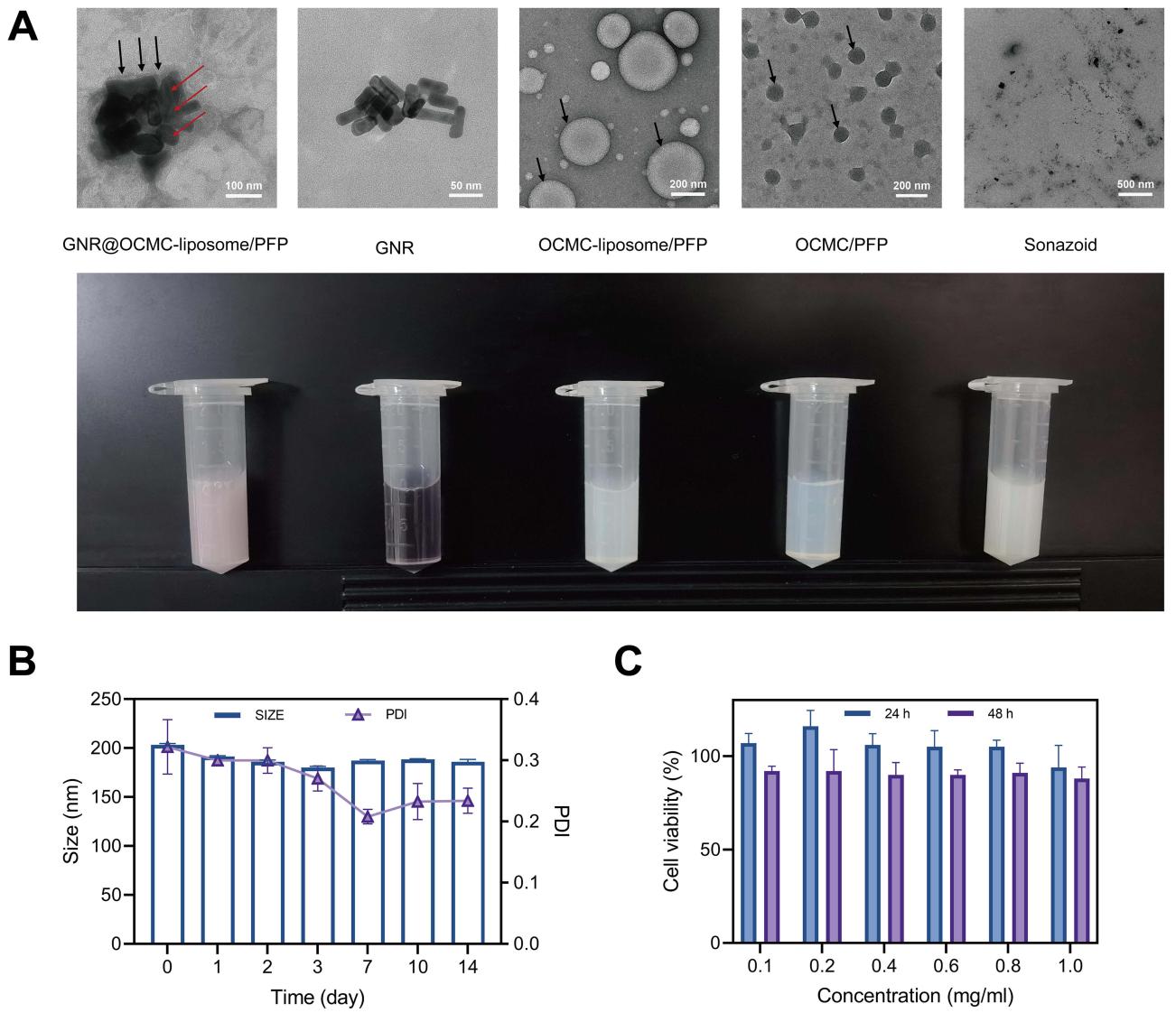

Figure 2 (**A**) TEM images alongside direct visual observations of the GNR@OCMC-liposome/PFP, GNR, OCMC-liposome/PFP, liposome/PFP and Sonazoid (shells marked with black arrows and cores marked with red arrows); (**B**) Plots showing of the size of GNR@OCMC-liposome/PFP and its PDI overtime at 4°C; (**C**) Changes in C2C12 cell viability after 24 hours and 48 hours incubation with the GNR@OCMC-liposome/PFP.

optimal temperature range between 40°C and 45°C was determined. Consequently, experimental conditions comprising a laser power density of 1.0W/ cm^2 and a solution concentration of 5 mg/mL were employed in this study.

Considering the temperature-dependent phase transition, the transition of GNR@OCMC-liposome/PFP from a liquid to a gas state was examined. The phase transition was observed under an optical microscope during NIR light irradiation (760 nm, 1.0 W/cm^2, 5 min). As depicted in Figure 3D, due to its small particle size, the specific morphology of the GNR@OCMC-liposome/PFP was not discernible before irradiation under the microscope. However, following irradiation, there was a significant increase in the number of MBs, accompanied by a gradual enlargement in their diameter as observed through microscopy. These observations indicate that the GNR@OCMC-liposome/PFP demonstrates efficient MB generation upon excitation with an NIR light source and holds potential as a promising contrast agent for ultrasound imaging.

Ultrasound Imaging Capability

As depicted in Figure 4A, the GNR@OCMC-liposome/PFP demonstrated an excellent ultrasound imaging ability akin to that of Sonazoid, in contrast to the PBS and GNR@OCMC-liposome groups without PFP, which showed no significant

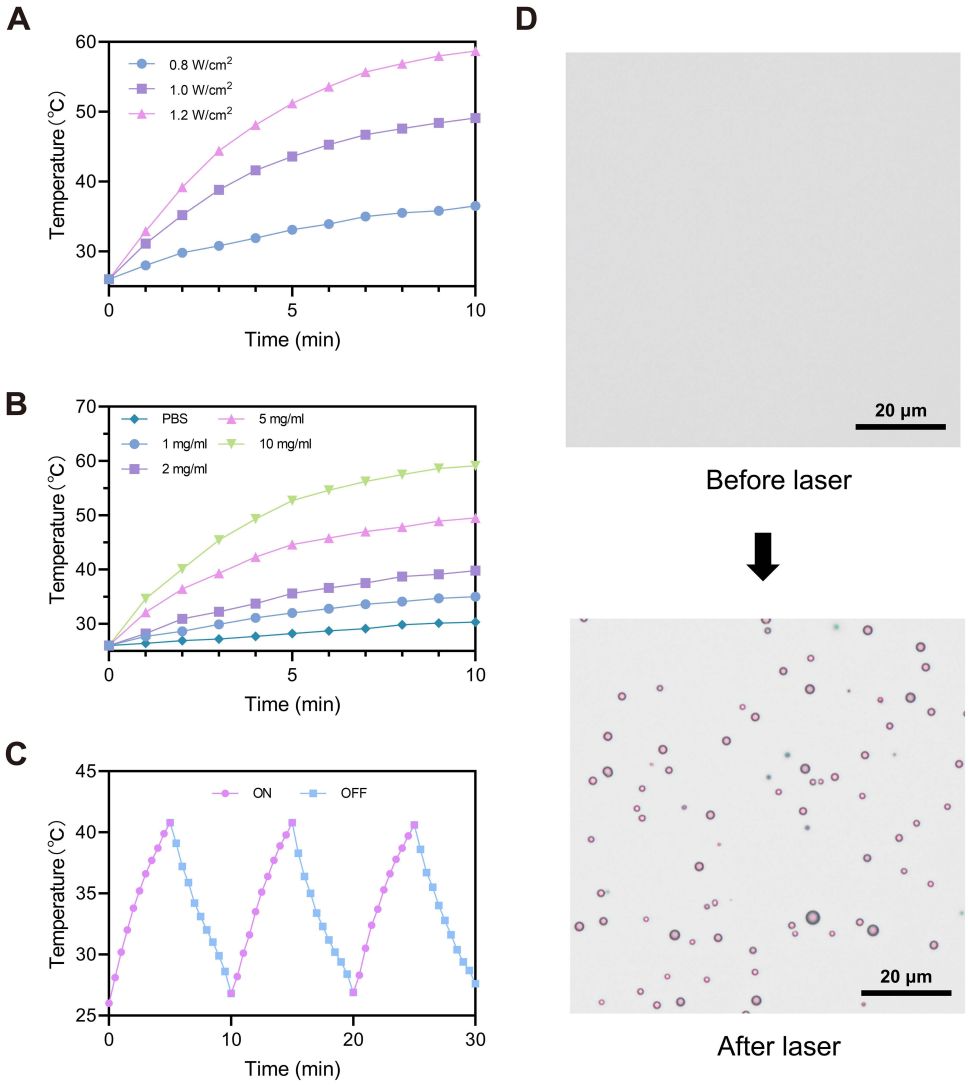

Figure 3 Photothermal properties of the GNR@OCMC-liposome/PFP and its phase transition behavior. (**A**) Temperature changes of the GNR@OCMC-liposome/PFP under various power densities of 760 nm laser for 10 minutes. (**B**) Temperature changes of different concentrations of GNR@OCMC-liposome/PFP under 760 nm laser irradiation for 10 min. (**C**) Temperature-time profiles of the GNR@OCMC-liposome/PFP after irradiation by a 760 nm laser (1.0 W/cm^2) for 3 on-off cycles. (**D**) Phase transition micrographs of the GNR@OCMC-liposome/PFP after irradiation with a 760 nm NIR laser. Scale bar=20 μm.

ultrasound echo signal. A quantitative analysis (Figure 4C) revealed that the echo intensity from the GNR@OCMC-liposome/PFP was comparable to that of Sonazoid, whereas the signal intensity from both the PBS and GNR@OCMC-liposome groups was significantly weaker.

After confirming the GNR@OCMC-liposome/PFP in vitro imaging capability, subsequent in vivo experiments were conducted. The imaging efficacy of GNR@OCMC-liposome/PFP is dependent on the generation of MBs, with ODV facilitating the transformation of NPs into MBs for ultrasound imaging purposes. Upon intravenous administration and subsequent NIR light irradiation on the hindlimbs of mice, ultrasound images were captured in both two-dimensional B-mode and CEUS mode. Illustrated in Figure 4B, the oval dashed box denotes the perfusion area within mouse hindlimb muscles, where no significant CEUS signal was observed in mice receiving PBS or GNR@OCMC-liposome injections; white arrows highlight MB echoes in the perfused zones. The Sonazoid group displayed pronounced ultrasound contrast in the hindlimb muscles, whereas the GNR@OCMC-liposome/PFP group showed limited contrast, with only scattered MBs diffusion found in the blood vessels and muscle tissues. Figure 4D presents a quantitative assessment of ultrasound intensity across a specified muscle region, displaying similar intensities between the PBS and GNR@OCMC-liposome groups, lacking in vivo CEUS effects. However, significant differences were observed upon comparison with the GNR@OCMC-liposome/PFP.

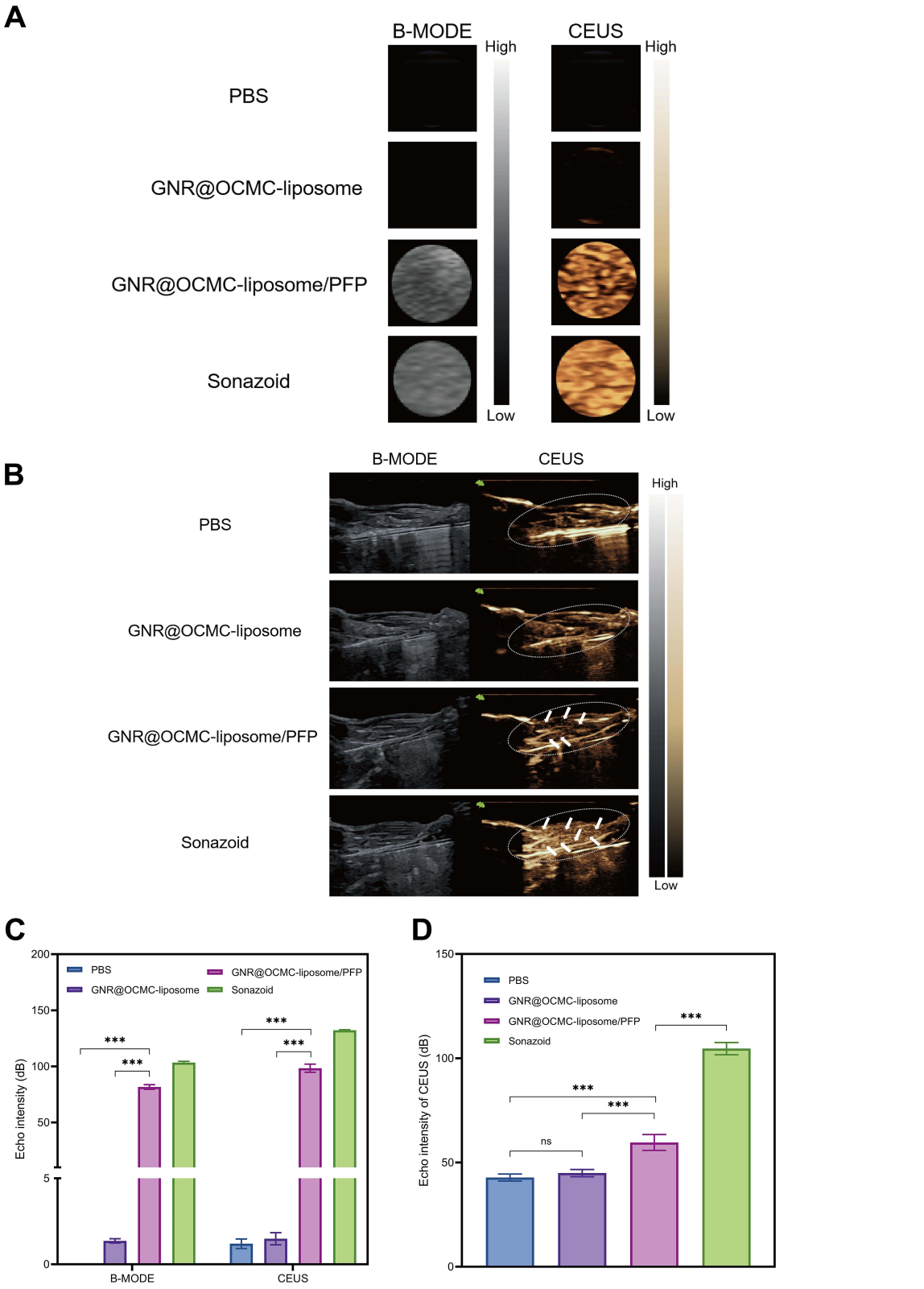

Figure 4 Ultrasound imaging capability of the GNR@OCMC-liposome/PFP. (**A**) B-mode and CEUS images of PBS, GNR@OCMC-liposome, GNR@OCMC-liposome/PFP, and Sonazoid groups; (**B**) B-mode and CEUS images of longitudinal sections of hindlimb muscles after a tail vein injection of PBS, GNR@OCMC-liposome, GNR@OCMC-liposome/PFP or Sonazoid in mice irradiated with NIR light (the oval dashed box area highlights the perfusion range of the mouse hindlimb muscles, while the white arrows indicate the MB echoes in the perfused area); (**C**) Quantification values of the echo intensity corresponding to the various modality ultrasound images in (**A**); (**D**) Quantification values of the echo intensity corresponding to the CEUS images in (**B**). ***Indicates $P < 0.001$ while ns indicates that the difference was not statistically significant.

Photothermal Imaging Capability

Figure 5A illustrates that both the GNR@OCMC-liposome group and the GNR@OCMC-liposome/PFP, when loaded with GNRs, demonstrated notable photothermal responsiveness in vitro experiments. These groups exhibited a continuous temperature increase over time, reaching approximately 40°C in about 5 minutes, a threshold deemed suitable for mild

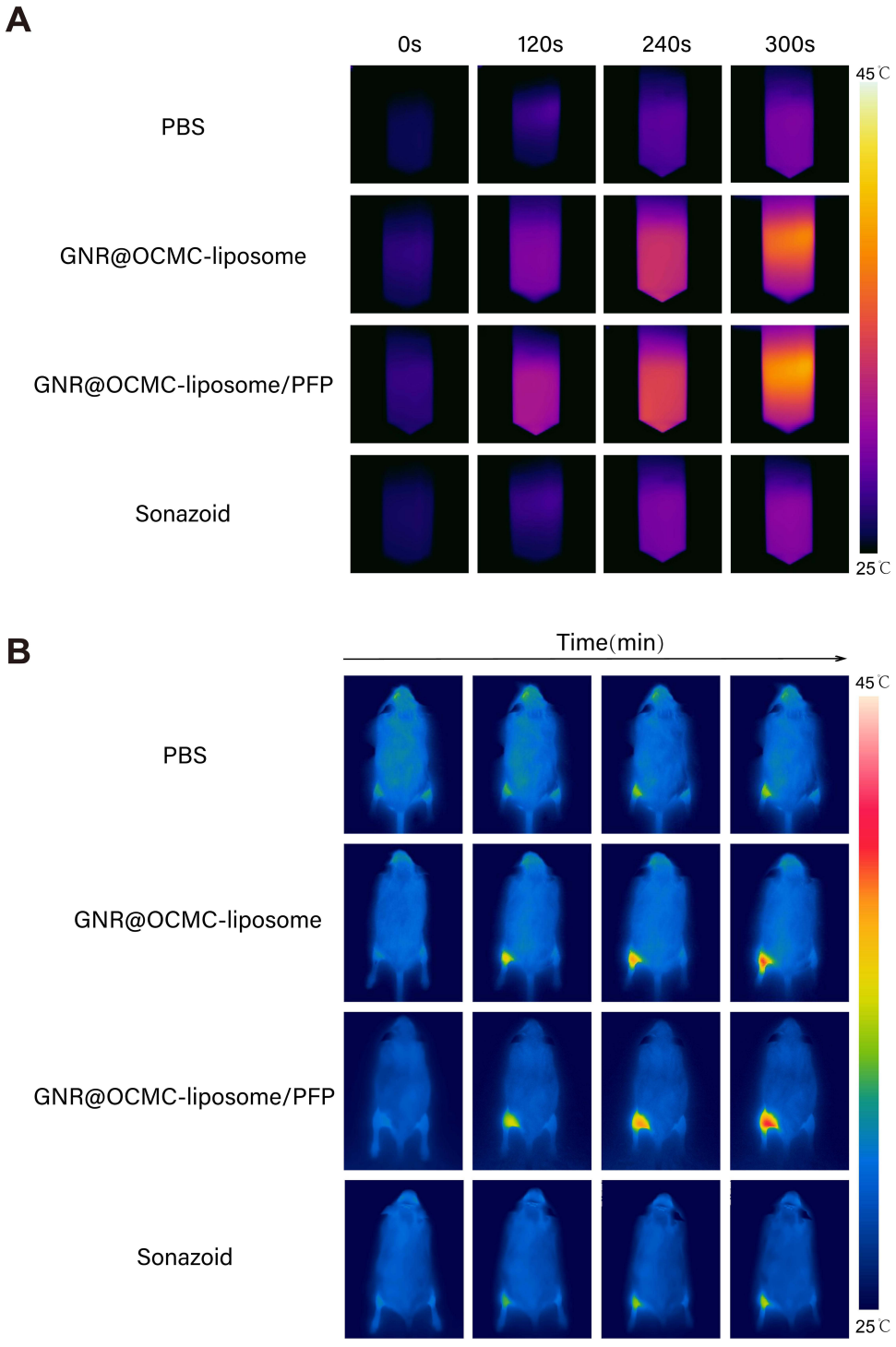

Figure 5 Photothermal imaging capability of the GNR@OCMC-liposome/PFP. (**A**) Photothermal images of PBS, GNR@OCMC-liposome, GNR@OCMC-liposome/PFP and Sonazoid groups under NIR irradiation (760 nm, 1.0 W/cm^2); (**B**) Photothermal images of the left hindlimb of mice after tail vein injection of PBS, GNR@OCMC-liposome, GNR@OCMC-liposome/PFP and Sonazoid irradiated by the NIR laser over time.

photothermal treatment.[17] In contrast, only negligible warming was observed in the PBS and Sonazoid groups; attributed to the physical thermal effects of NIR light irradiation.

Following intravenous injection of a 100 μL volume containing PBS, GNR@OCMC-liposome, GNR@OCMC-liposome/PFP, and Sonazoid, photothermal imaging was performed at various intervals. As shown in Figure 5B, NIR light was applied to the left hindlimbs of the mice, while the right hindlimbs served as controls. The results highlighted that both the GNR@OCMC-liposome and GNR@OCMC-liposome/PFP groups exhibited enhanced in vivo photothermal imaging capabilities, consistent with the in vitro findings, suggesting the suitability of the GNR@OCMC-liposome/PFP as a bimodal NCA.

Photothermal Treatment of Ischemic Hindlimbs in Mice

With reference to previous work,[18] the hindlimb ischemia was simulated through the ligation of lower limb vessels. As depicted in Figure 6A, ischemic mice exhibited mild swelling and reduced mobility in the left hindlimb on postoperative day 1. Histological analysis, as seen in Supplementary Figure 4, revealed significant differences between the muscle tissues of sham-operated and ischemic mice. Sham-operated mice displayed regularly aligned muscle fibers with consistent cell size and extracellular interstitial space, devoid of noticeable infiltration by inflammatory cells. Conversely, the affected limbs of ischemic mice exhibited myocyte swelling, structural disorganization of muscle bundles, reticular dilatation of capillaries, and some infiltration of inflammatory cells as soon as 1 day post-surgery. Subsequently, necrotic-like pathological changes appeared on day 7, with H&E staining showing a significant decrease in myocytes, disappearance of most nuclei due to nucleolysis, necrotic and atrophic myofibers with irregular morphology, increased cellular gaps, and connective tissue proliferation. By postoperative day 7, the left hindlimb of ischemic mice exhibited conspicuous purple-black discoloration and significant muscle atrophy when compared to their contralateral healthy limb (Figure 6A); whereas the incision site in the left hindlimb of sham-operated mice had healed well without notable disparity between both lower limbs. These findings confirm that we successfully established the mouse model for left hindlimb ischemia.

Due to limitations in obtaining accurate intensity data from ultrasonography of mouse hindlimb muscles using GNR@OCMC-liposome/PFP, pathologic findings were relied upon as the primary measure of treatment effectiveness. Moreover, CD31, identified as Platelet Endothelial Cell Adhesion Molecule-1 (PECAM-1) and serving as an indicator of vascular endothelial integrity, in conjunction with α-smooth muscle actin (α-SMA), acknowledged as a definitive marker for myofibroblasts, are integral to capillary neoformation and muscular regeneration.[19,20] Consequently, to evaluate the effectiveness of photothermal therapy in ischemic hindlimbs of mice, quantitative immunofluorescence assays targeting CD31 and α-SMA were performed.

To assess the effectiveness of the proposed intervention in enhancing recovery from ischemic muscle injury, mice were systematically allocated into three experimental groups: PBS, PBS + laser, and GNR@OCMC-liposome/PFP + laser. The treatment was conducted over seven days, as outlined in the flowchart in Figure 6B. The PBS group, which did not receive laser irradiation, exhibited signs of bruising and suboptimal muscle recovery in the affected limbs following treatment. Conversely, the PBS + laser group demonstrated marginally better muscle recovery, attributed to the slight elevation in local temperature induced by laser exposure, which presumably enhanced blood flow to some extent. In contrast, the introduction of GNR@OCMC-liposome/PFP followed by targeted photothermal therapy markedly alleviated muscle deterioration. Histological analysis using H&E staining on the seventh day, revealed a pronounced increase in neoformed myofibroblasts and neocapillaries within the lesion site in the GNR@OCMC-liposome/PFP + laser group (Figure 6F). This observation was corroborated by immunohistochemical analysis for CD31 (Supplementary Figure 5A) and dual immunofluorescence staining for CD31 and α-SMA (Figure 6C). Quantitative analyses focusing on the expression levels of CD31 and α-SMA in the GNR@OCMC-liposome/PFP + laser group revealed statistically significant differences when compared to the other two groups (Figure 6D and E, Supplementary Figure 5B). Additionally, comparative histological assessments, including H&E and Masson's trichrome staining (Figure 6F), revealed severe myocyte depletion, nuclear dissolution, pronounced necrosis, and disintegration of muscular architecture in the PBS group. This pathology was characterized by widened muscle spaces, loss of myofibril bundling, size variability among myofibrils, and vacuolation of the cytoplasm. Although the PBS + laser group showed some signs of myofibril regeneration, the abundance of neonatal myogenic cells and capillaries was significantly lower than that observed in

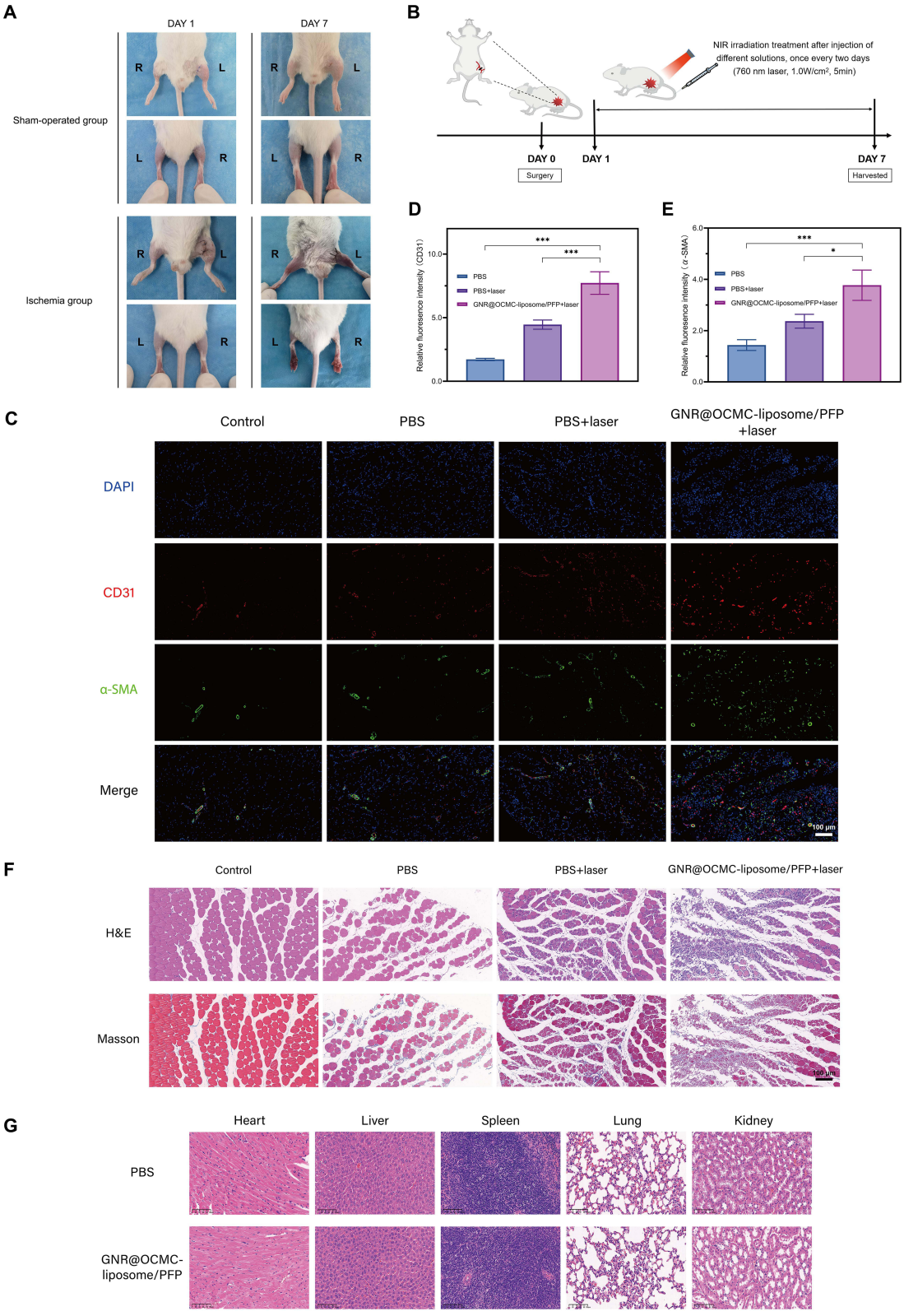

Figure 6 Modeling validation and therapeutic procedures and effects in ischemic mice. (**A**) Visual observation of both hindlimbs on postoperative days 1 and 7 in sham-operated and ischemia groups; (**B**) Flowchart of treatment of ischemic mice; (**C**) Double immunofluorescence images showing CD31 (red) and α-SMA (green) in the muscles of the left hindlimb of healthy control and variously treated ischemic mice, with nuclei stained by DAPI (blue); (**D** and **E**) Quantification of CD31 (**D**) and α-SMA (**E**) in (**C**); (**F**) The results of H&E staining and Masson's trichrome staining of the left hindlimb muscles of ischemic mice at day 7 following various treatments; (**G**) H&E staining results of major organs in mice treated with PBS and GNR@OCMC-liposome/PFP. *Indicates $P < 0.05$ and ***Indicates $P < 0.001$. Scale bar=100 μm.

the GNR@OCMC-liposome/PFP + laser group. These findings indicate that without timely and effective intervention following skeletal muscle injury at day 7, there is a significant decrease in myocyte count accompanied by irreversible necrosis which hinders proper functional muscle recovery.

Within the critical initial week following ischemia-induced skeletal muscle injury, GNR@OCMC-liposome/PFP demonstrated a remarkable ability to expedite the recovery of ischemic muscle tissue through sequential photothermal treatments. The underlying mechanism is attributed primarily to the photothermal efficacy of the gold nanocore, which significantly improved blood circulation within the affected limb areas of mice, thereby facilitating their rehabilitation. Notably, this therapeutic approach was associated with minimal adverse effects on the skin and muscle tissues, affirming that mild photothermal therapy does not cause localized tissue damage.

Finally, the biocompatibility profile of the GNR@OCMC-liposome/PFP was evaluated through histological examination using H&E staining of major organs (Figure 6G), revealing no detectable histopathological abnormalities. Moreover, comprehensive assessments conducted 48 hours following the injection of the GNR@OCMC-liposome/PFP and PBS revealed no significant differences in all major hematological and biochemical markers in mice treated with GNR@OCMC-liposome/PFP, as compared to the PBS control group (Supplementary Figure 6). These findings align with the outcomes of in vitro toxicity studies, collectively highlighting the excellent biocompatibility of GNR@OCMC-liposome/PFP.

Discussion

Skeletal muscle, being among the organs with the highest blood flow requirements, is particularly vulnerable to lower limb ischemia conditions such as fascial compartment syndrome and muscle necrosis, potentially leading to amputation or life-threatening complications.[21] The diagnostic and therapeutic significance of microvascular perfusion imaging in skeletal muscle is thus crucial for the healing and rehabilitation of limb and ischemic muscle injuries. The integration of nanotechnology, materials science, and medicine has revolutionized clinical treatment approaches by enabling NPs to offer targeted delivery, diagnostic imaging, and therapeutic functionalities, all while adhering to stringent biosafety protocols.[22]

In this study, we synthesized GNR@OCMC-liposome/PFP as an NCA that integrates diagnostic and therapeutic capabilities for musculoskeletal disorders. This NCA exhibited a homogeneous surface morphology, good dispersion in aqueous solutions, and an average size of approximately 200 nm, significantly smaller than the commercially available UCA Sonazoid, facilitating its effective reach within terminal microcirculation. The negative ζ potential of GNR@OCMC-liposome/PFP contributes to its stability and prevents aggregation, showcasing its potential in microcirculatory perfusion assessment and facilitation of blood circulation during diagnosis.

To date, a diverse array of photosensitive materials has found extensive application in cutting-edge fields such as photoacoustic imaging. Among these materials, gold nanomaterials demonstrate efficient photothermal conversion through SPR, while GNRs exhibit excellent plasma properties and biocompatibility.[23] In this study, the synthesized NPs not only integrated GNRs as the core but also effectively encapsulated them with the phase transition material PFP. PFP, a liquid fluorocarbon material with a boiling point of 27°C,[24] undergoes ODV under specific conditions of light irradiation, where photothermal materials absorb and convert light energy into heat energy. Upon reaching the boiling point of PFP, a phase transition occurs, transforming the liquid core of nanodroplets into gas cores, thereby forming MBs. This process enhances acoustic impedance in irradiated tissues, thereby improving local visualization effects for CEUS.[25,26] However, when PFP is encapsulated by different materials such as lipids or other polymers, the Laplace force leads to an increased vaporization threshold for liquid-core PFP posing challenges for ODV.[27,28]

Liposomes have gained widespread recognition for their application safety over recent decades;[29] however, they often exhibit loose surfaces with voids that cannot be stably preserved over time. In contrast, due to its rigid shell nature, OCMC can effectively penetrate these surface voids on liposomes, thereby enabling superior gas encapsulation for ultrasound imaging and enhanced biocompatibility. Building upon this concept, our study innovatively combines OCMC (with rigid shell) with liposomes (with soft shell) to form a composite nano contrast shell. This composite shell exhibits a lower collapse pressure compared to a single shell[30] and is capable of inducing phase transition under ODV conditions while achieving therapeutic effects that promote blood circulation at an appropriate temperature.

Using NIR light irradiation of GNR@OCMC-liposome/PFP for 5 minutes (optimal conditions for ODV and CEUS), the liquid fluorocarbon NPs were observed to undergo a liquid-gas phase transition, thereby exhibiting contrast enhancement capability.[31] Theoretically, CEUS employs a low mechanical index imaging modality that enables precise visualization of the contrast agent's entry into the skeletal muscle by effectively suppressing the signal from surrounding tissues resulting in the appearance of a flowing dot or strip with medium to high echogenicity within the skeletal muscle.[32] However, during the actual imaging process, only sporadic ultrasonic signals were observed in the hindlimb muscles of mice during the actual imaging process, potentially attributed to the increased difficulty of ODV while prioritizing nanosystem cyclic stability. Therefore, achieving a delicate balance between ODV difficulty and nanodroplet stability in cycling poses a challenging issue. Consequently, optimizing the preparation process and exploring imaging conditions in future studies are imperative for improved NP loading efficiency, thereby reducing ODV difficulty and enhancing imaging efficacy.

The local effects of perfusion are believed to contribute significantly to the beneficial therapeutic effect of ultrasound in tissue repair and healing.[33] Low-frequency ultrasound has demonstrated its potential in enhancing tissue perfusion in animal models of limb and myocardial ischemia.[34] In recent years, several studies have shown the positive implications of preparing nanoscale ultrasound contrast agent (nUCA) for targeted treatment in musculoskeletal injury lesions, especially in ischemic diseases.[35,36] Currently, the research on multifunctional contrast agents designed based on NPs is still in its nascent stages. In this study, we aimed to develop a multifunctional UCA suitable for assessing microcirculatory perfusion of the musculoskeletal system along with photothermal therapy. Furthermore, our experimental findings demonstrated that localized mild photothermal treatment using this system for a short duration improved or even reversed ischemic muscle damage, as confirmed by the distribution of microvascular density, indicating some therapeutic angiogenic effects.

It is anticipated that such multifunctional nUCAs can be utilized in various cases of lower extremity ischemic diseases, owing to their ultra-small particle size facilitating enhanced penetration through blood blockages and targeting poorly perfused lesions. Furthermore, they offer a unique fine image contrast effect and satisfactory differentiation in the advancement of high-resolution ultrasonography and related algorithms, which proves challenging with current commercially available micron-sized UCAs.

The integration of these emerging technologies with multifunctional nanocarriers will significantly expand their biomedical applications. These NCAs can be utilized for prolonged drug or gene delivery to ischemic regions characterized by poor microcirculatory perfusion, facilitated by multimodal imaging techniques such as photoacoustic imaging, ultrasound therapeutic effects like ultrasonic cavitation effects, and even employed as carriers for targeted drug or gene delivery to ischemic areas. Despite the promising ultrasound contrast and photothermal imaging capabilities exhibited by the synthesized NCAs in controlled in vitro conditions, their performance in vivo under complex physiological conditions remains less than optimal. This necessitates further exploration and refinement of both their synthesis and in vivo imaging protocols. Additionally, a comprehensive assessment of the long-term toxicity of NCAs is imperative to mitigate safety concerns currently hampering their clinical application. Furthermore, delineating the mechanisms through which localized photothermal therapy augments systemic blood circulation for enhanced therapeutic efficacy, along with verifying the medium- and long-term effectiveness of this treatment modality as demonstrated in our study, are areas that require further investigation.

Conclusion

In this study, we successfully synthesized an NCA loaded with GNR and PFP, which can be activated by NIR light. It also demonstrates a uniform morphology, small particle size, and a robust biocompatibility profile. Initially, we deployed this NCA to assess the microcirculatory perfusion of the musculoskeletal system via both in vitro and in vivo studies. Its dual-imaging functionality, integrating ultrasound and photothermal techniques, and the optimized particle dimension facilitate effective penetration into the terminal microcirculation. Upon exposure to 760 nm NIR light, PFP undergoes a liquid-to-gas phase transition, augmenting ultrasound imaging. Concurrently, NIR laser activation promotes local blood flow, thereby enhancing microcirculatory perfusion and enhancing rehabilitation treatments. Furthermore, the NCA demonstrated outstanding biocompatibility in both in vitro and in vivo experiments. Building on previous nano-ultrasound imaging research, this study endeavors to introduce innovative approaches and methods for the treatment of ischemic muscle conditions, progressing toward comprehensive diagnosis and precision treatments.

Abbreviations

APS, Ammonium persulfate; α-SMA, α-smooth muscle actin; CCK-8, Cell Counting Kit 8; CDFI, color Doppler flow imaging; CEUS, contrast-enhanced ultrasound; CTAB, cetyltrimethy-lammonium bromide; DMEM, Dulbecco's modified Eagle's medium; FBS, Fetal Bovine Serum; GNR, gold nanorod; H&E, haematoxylin and eosin; MB, microbubble; MMA, Methyl methacrylate; NCA, nano-contrast agent; NIR, near-infrared; NP, nanoparticle; nUCA, nanoscale ultrasound contrast agent; OCMC, O-carboxymethyl chitosan; ODV, optical droplet vaporization; PBS, Phosphate Buffered Saline; PDI, polydispersity index; PECAM-1, Platelet Endothelial Cell Adhesion Molecule-1; PFP, perfluoropentane; POPC, 1-palmitoyl-2-oleoyl-sn-glycero-3-phosphocholine; SPR, surface plasmon resonance; TEM, transmission electron microscopy; UCA, ultrasound contrast agent.

Acknowledgments

This research was sponsored by the National Natural Science Foundation of China (81501492), the Natural Science Foundation of Shanghai of China (20ZR1457900), Program of Shanghai Academic Research Leader (22XD1404700), the Three-year Action Plan of Talent Construction of Changzheng Hospital, Military Medical Talent Project of Pyramid Talent Project, Science and Technology Initiation Special Program of Shanghai Fourth People's Hospital of Tongji University (SYKYQD06101), Medical Research Project of Shanghai Hongkou District Health Commission (2302-26) and Clinical Key Supporting Project of Health Commission of Shanghai Hongkou District (HKLCFC202404). The authors would like to express their gratitude to EditSprings (https://www.editsprings.cn) for the expert linguistic services provided.

Disclosure

The authors declare no conflicts of interest in this work.

References

1. Dunford EC, Au JS, Devries MC, Phillips SM, MacDonald MJ. Cardiovascular aging and the microcirculation of skeletal muscle: using contrast-enhanced ultrasound. *Am J Physiol Heart Circulatory Physiol*. 2018;315(5):H1194–h1199. doi:10.1152/ajpheart.00737.2017
2. Hotfiel T, Hoppe MW, Heiss R, et al. Quantifiable contrast-enhanced ultrasound explores the role of protection, rest, ice (Cryotherapy), compression and elevation (PRICE) therapy on microvascular blood flow. *Ultrasound Med Biol*. 2021;47(5):1269–1278. doi:10.1016/j.ultrasmedbio.2021.01.003
3. Kunz P, Kiesl S, Groß S, Kauczor HU, Schmidmaier G, Fischer C. Intra-observer and device-dependent inter-observer reliability of contrast-enhanced ultrasound for muscle perfusion quantification. *Ultrasound Med Biol*. 2020;46(2):275–285. doi:10.1016/j.ultrasmedbio.2019.10.007
4. Doll J, Waizenegger S, Schmidmaier G, Weber MA, Fischer C. Contrast-enhanced ultrasound: a viable diagnostic tool in predicting treatment failure after non-union revision surgery for upper- and lower-limb non-unions. *Ultrasound Med Biol*. 2021;47(11):3147–3158. doi:10.1016/j.ultrasmedbio.2021.07.020
5. Fischer C, Haug T, Weber MA, Kauczor HU, Bruckner T, Schmidmaier G. [Contrast-Enhanced Ultrasound (CEUS) Identifies Perfusion Differences Between Tibial Fracture Unions and Non-Unions]. Kontrastmittelverstärkter Ultraschall (CEUS) zur Beurteilung der tibialen Knochenperfusion bei physiologischer und gestörter Frakturheilung mit Pseudarthrosenbildung. *Ultraschall der Medizin*. 2020;41(1):44–51. German. doi:10.1055/a-0637-1679
6. Kim GW, Kang C, Oh YB, Ko MH, Seo JH, Lee D. ultrasonographic imaging and anti-inflammatory therapy of muscle and tendon injuries using polymer nanoparticles. *Theranostics*. 2017;7(9):2463–2476. doi:10.7150/thno.18922
7. Zhang W, Zang Y, Lu Y, Han J, Xiong Q, Xiong J. Photothermal effect and multi-modality imaging of up-conversion nanomaterial doped with gold nanoparticles. *Int J Mol Sci*. 2022;23(3):1.
8. Shang H, Gu H, Zhang N. From traditional to novel treatment of arthritis: a review of recent advances in nanotechnology-based thermal therapy. *Nanomedicine*. 2021;16(23):2117–2132. doi:10.2217/nnm-2021-0182
9. Shan H, Zhou X, Tian B, et al. Gold nanorods modified by endogenous protein with light-irradiation enhance bone repair via multiple osteogenic signal pathways. *Biomaterials*. 2022;284:121482. doi:10.1016/j.biomaterials.2022.121482
10. Wu Y, Liao Q, Wu L, et al. ZnL(2)-BPs integrated bone scaffold under sequential photothermal mediation: a win-win strategy delivering antibacterial therapy and fostering osteogenesis thereafter. *ACS nano*. 2021;15(11):17854–17869. doi:10.1021/acsnano.1c06062
11. Yang D, Ni Y, Kong X, et al. Self-healing and elastic triboelectric nanogenerators for muscle motion monitoring and photothermal treatment. *ACS nano*. 2021;15(9):14653–14661. doi:10.1021/acsnano.1c04384
12. Zhang F, Hou Y, Zhu M, et al. Death pathways of cancer cells modulated by surface molecule density on gold nanorods. *Adv Sci*. 2021;8(22):e2102666. doi:10.1002/advs.202102666
13. Kim HS, Lee DY. Near-infrared-responsive cancer photothermal and photodynamic therapy using gold nanoparticles. *Polymers*. 2018;10(9):961. doi:10.3390/polym10090961
14. Wang L, Lu H, Gao Q, et al. A multifunctional theranostic contrast agent for ultrasound/near infrared fluorescence imaging-based tumor diagnosis and ultrasound-triggered combined photothermal and gene therapy. *Acta Biomater*. 2019;99:373–386. doi:10.1016/j.actbio.2019.09.015
15. Xi Y, Pan W, Liu Y, et al. α-Lipoic acid loaded hollow gold nanoparticles designed for osteoporosis treatment: preparation, characterization and in vitro evaluation. *Artif Cells Nanomed Biotechnol*. 2023;51(1):131–138. doi:10.1080/21691401.2022.2149542

16. Li X, Lovell JF, Yoon J, Chen X. Clinical development and potential of photothermal and photodynamic therapies for cancer. *Nat Rev Clin Oncol*. 2020;17(11):657–674. doi:10.1038/s41571-020-0410-2
17. Zhang X, Cheng G, Xing X, et al. Near-infrared light-triggered porous AuPd alloy nanoparticles to produce mild localized heat to accelerate bone regeneration. *J Phys Chem Lett*. 2019;10(15):4185–4191. doi:10.1021/acs.jpclett.9b01735
18. Belcik JT, Davidson BP, Xie A, et al. Augmentation of Muscle Blood Flow by Ultrasound Cavitation Is Mediated by ATP and Purinergic Signaling. *Circulation*. 2017;135(13):1240–1252. doi:10.1161/circulationaha.116.024826
19. Zhao YC, Guo W, Gao BH. Hypoxic training upregulates mitochondrial turnover and angiogenesis of skeletal muscle in mice. *Life Sci*. 2022;291:119340. doi:10.1016/j.lfs.2021.119340
20. Elbialy ZI, Assar DH, Abdelnaby A, et al. Healing potential of Spirulina platensis for skin wounds by modulating bFGF, VEGF, TGF-ß1 and α-SMA genes expression targeting angiogenesis and scar tissue formation in the rat model. *Biomed Pharmacothe*. 2021;137:111349. doi:10.1016/j.biopha.2021.111349
21. Chen L, Ma H, Liu H, et al. Quantitative photoacoustic imaging for early detection of muscle ischemia injury. *Am J Transl Res*. 2017;9(5):2255–2265.
22. Hsu JC, Tang Z, Eremina OE, et al. Nanomaterial-based contrast agents. *Nat Rev Method Primers*. 2023;3(1):30. doi:10.1038/s43586-023-00211-4
23. Tian Y, Liu Z, Tan H, et al. New Aspects of Ultrasound-Mediated Targeted Delivery and Therapy for Cancer. *Int j Nanomed*. 2020;15:401–418. doi:10.2147/ijn.S201208
24. Li M, Bian X, Chen X, et al. Multifunctional liposome for photoacoustic/ultrasound imaging-guided chemo/photothermal retinoblastoma therapy. *Drug Delivery*. 2022;29(1):519–533. doi:10.1080/10717544.2022.2032876
25. Liu WW, Huang SH, Li PC. Synchronized optical and acoustic droplet vaporization for effective sonoporation. *Pharmaceutics*. 2019;11(6):1.
26. Zhang Q, Yang Y, Xue H, et al. Intensified and controllable vaporization of phase-changeable nanodroplets induced by simultaneous exposure of laser and ultrasound. *Ultrason Sonochem*. 2023;94:106312. doi:10.1016/j.ultsonch.2023.106312
27. Hanieh PN, Ricci C, Bettucci A, et al. Ultrastable shelled PFC nanobubbles: a platform for ultrasound-assisted diagnostics, and therapy. *Nanomedicine*. 2022;46:102611. doi:10.1016/j.nano.2022.102611
28. Tamarov K, Sviridov A, Xu W, et al. Nano air seeds trapped in mesoporous janus nanoparticles facilitate cavitation and enhance ultrasound imaging. *ACS Appl Mater Interfaces*. 2017;9(40):35234–35243. doi:10.1021/acsami.7b11007
29. Hallan SS, Amirian J, Brangule A, Bandere D. Lipid-based nano-sized cargos as a promising strategy in bone complications: a review. *Nanomaterials*. 2022;12(7):1146. doi:10.3390/nano12071146
30. Li Z, Lai M, Zhao S, et al. Ultrasound molecular imaging for multiple biomarkers by serial collapse of targeting microbubbles with distinct acoustic pressures. *Small*. 2022;18(22):e2108040. doi:10.1002/smll.202108040
31. Yu M, Xu X, Cai Y, Zou L, Shuai X. Perfluorohexane-cored nanodroplets for stimulations-responsive ultrasonography and O(2)-potentiated photodynamic therapy. *Biomaterials*. 2018;175:61–71. doi:10.1016/j.biomaterials.2018.05.019
32. Soman D, Hodovan J, Macon CJ, et al. Contrast ultrasound assessment of skeletal muscle recruitable perfusion after permanent left ventricular assist device implantation: implications for functional recovery. *J Am Soc Echocard*. 2022;35(5):495–502. doi:10.1016/j.echo.2021.12.014
33. Jiang X, Savchenko O, Li Y, et al. A review of low-intensity pulsed ultrasound for therapeutic applications. *IEEE Transact Bio Med Engine*. 2019;66(10):2704–2718. doi:10.1109/tbme.2018.2889669
34. Belcik JT, Mott BH, Xie A, et al. Augmentation of limb perfusion and reversal of tissue ischemia produced by ultrasound-mediated microbubble cavitation. *Circ Cardiovasc Imaging*. 2015;8(4). doi:10.1161/CIRCIMAGING.114.002979
35. Lee D, Bae S, Ke Q, et al. Hydrogen peroxide-responsive copolyoxalate nanoparticles for detection and therapy of ischemia-reperfusion injury. *J Controll Rel*. 2013;172(3):1102–1110. doi:10.1016/j.jconrel.2013.09.020
36. Jung E, Noh J, Kang C, Yoo D, Song C, Lee D. Ultrasound imaging and on-demand therapy of peripheral arterial diseases using H(2)O(2)-Activated bubble generating anti-inflammatory polymer particles. *Biomaterials*. 2018;179:175–185. doi:10.1016/j.biomaterials.2018.07.003